J. Fluid Mech. (2011), *vol.* 668, *pp.* 582–606.
doi:10.1017/S0022112010005343

Oblique runup of non-breaking solitary waves on an inclined plane

GEIR K. PEDERSEN†

Department of Mathematics, University of Oslo, PO Box 1053, 0316, Oslo, Norway

(Received 24 August 2010; revised 24 September 2010; accepted 5 October 2010)

When a wave of permanent form is obliquely incident on an inclined plane, the wave pattern becomes stationary in a frame of reference which moves along the shore. This enables a simplified mathematical description of the problem which is used herein as a basis for efficient and accurate numerical simulations. First, a nonlinear and weakly dispersive set of Boussinesq equations for the downstream evolution of such stationary patterns is derived. In the hydrostatic approximation, streamline-based Lagrangian versions of the evolution equations are developed for automatic tracing of the shoreline. Both equation sets are, in their present form, developed for non-breaking waves only. Finite difference models for both equation sets are designed. These methods are then coupled dynamically to obtain a single nonlinear model with dispersive wave propagation in finite depth and an accurate runup representation. The models are tested by runup of waves at normal incidence and comparison with a more general model for the refraction of a solitary wave on a slope. Finally, a set of runup computations for oblique solitary waves is performed and compared with estimates of oblique runup heights obtained from a combination of an analytic solution for normal incidence and optics. We find that the runup heights decrease in proportion to the square of the angle of incidence for angles up to 45°, for which the height is reduced by around 12 % relative to that of normal incidence. In Appendix A, the validity of the downstream formulation is discussed in the light of solitary wave optics and wave jumps.

Key words: coastal engineering, solitary waves

1. Introduction

Today, runup on sloping beaches is included in standard models for tsunamis and long waves in coastal waters (Imamura 1996; Titov & Synolakis 1998; Kennedy *et al.* 2000; Lynett, Wu & Liu 2002; LeVeque & George 2008). Still, there is a considerable activity linked to benchmarking and analysis of the performance of models for this crucial, final stage of onshore wave propagation (see, for instance, Liu, Yeh & Synolakis 2008). Hence, well-controlled runup solutions, obtained under idealized circumstances, are important both for model validation and for gaining insight into the dynamics of the runup phenomenon as such. The class of reference solutions that has received most attention is based on the so-called hodograph transformation for waves of normal incidence on a plane beach. In essence, this transformation reduces the nonlinear shallow-water (NLSW) equations to the corresponding linear

† Email address for correspondence: geirkp@math.uio.no

problem. The hodograph tradition goes back to Carrier & Greenspan (1958) and was revitalized by Synolakis (1987), who found a closed-form asymptotic solution for the runup of soliton-shaped waves. The technique has been generalized to piecewise linear topographies and channels of parabolic cross-sections by Kânoğlu & Synolakis (1998) and Choi *et al.* (2008), respectively. Analytical solutions for the runup of bores on an inclined plane are reported by Keller, Levine & Whitham (1960) and Shen & Meyer (1963).

Few simple solutions for runup on sloping beaches in two horizontal dimensions exist. The lowest two modes of nonlinear eigenoscillations in parabolic basins take on very simple spatial forms (see Thacker 1981). Perturbation solutions for edge waves have been derived and coupled nonlinearly to periodic incident waves, explaining beach cusp formation, among others (see, for instance, Guza & Davis 1974). Certain classes of waves incident on geometries with parallel coastline and isobathymetric lines produce permanently shaped wave patterns moving along the coast. The time and the alongshore coordinate may then be merged into a single variable, reducing the number of dimensions by one. This has been exploited in a few published articles on wave reflection and runup and will also be employed in the present study. Using linear shallow-water theory, Carrier & Noiseux (1983) investigated the reflection of Gaussian-shaped pulses, representing tsunamis, from straight coastlines and continental shelves. Assuming nearly normal incidence, Ryrie (1983) developed weakly three-dimensional nonlinear shallow-water equations where the alongshore flow was decoupled from the motion in the normal direction which was governed by the standard equation set for plane waves. This formulation was used for runup of bores. Since there is no coupling back from the alongshore to the normal flow, this procedure reproduces the runup of normal incidence. Brocchini & Peregrine (1996) combined the approximation of weak obliquity with the hodograph transformation for the motion in the direction normal to a plane beach and studied properties of the alongshore flow for periodic incident waves. Later, Brocchini (1998) applied a similar approach to incident solitary waves. Again, the runup itself was as for normal incidence due to the approximation of weak obliqueness. No study of this kind with strong obliqueness, and hence the variation of the runup heights with the angle of incidence, is available in the literature.

Theoretical studies are generally performed with incident waves that are periodic or solitary waves. Still, a few investigations have been performed for other shapes involving skewness, such as in Didenkulova *et al.* (2007), or N-type shapes that are more like tsunamis from earthquakes and slides (Tadepalli & Synolakis 1994; Carrier, Wu & Yeh 2003; Pritchard & Dickinson 2007). Even though they differ from most waves found in nature, solitary waves are much investigated in laboratories because they are easy to generate and identify. Normal incidence experiments on solitary wave runup have been reported by, among others, Hall & Watts (1953), Meyer & Taylor (1972), Synolakis (1987), Li & Raichlen (2001) and Jensen, Pedersen & Wood (2003). Experimental and theoretical investigations of solitary wave runup on a conical island were published by Liu *et al.* (1995) and Briggs *et al.* (1995).

The main focus of the present article is oblique runup of solitary waves on an inclined plane, including full nonlinearity and weak dispersion. In a moving frame of reference, following the point of maximum runup transversely along the beach, the wave pattern becomes stationary in this case. Among others, Pedersen (1988) studied the stationary nonlinear pattern of diverging waves from a supercritical disturbance by downstream integration of a Boussinesq-type equation. Here, related Boussinesq and shallow-water equations are developed for downstream integration of stationary pattern in variable topography. A major gain, in comparison to solving corresponding equations in two horizontal dimensions and time, is the reduction of the problem to involve only one spatial and one time-like independent coordinate. This again allows for huge computational domains and makes complicated seaward input/radiation conditions superfluous.

A number of different numerical approaches for runup on sloping beaches have been published, displaying a large diversity concerning purpose as well as performance (see Pedersen 2008*b*). Tentatively, we may divide the methods into two groups. One with emphasis on ruggedness and simple invocation to real applications and another where the focus is on high accuracy and detailed investigation of more theoretical problems. Often, the models of the latter group are based on transformations and deforming grids for accurate treatment of the moving shoreline, while the former generally trace the shoreline in a fixed grid. Our strategy is to dynamically couple a fixed grid method in finite depth to a moving grid method near-shore.

In § 2, we first describe the nature of the stationary wave patterns emerging when solitary waves are incident on a straight beach. Then, the nonlinear and weakly dispersive Boussinesq equations are transformed for non-breaking waves, accordingly, to a new form involving the normal-beach coordinate and a time-like coordinate. This equation set is the basis for the fixed grid model mentioned above. Next, the nonlinear shallow-water parts of the transformed equations are re-transformed by the introduction of Lagrangian-type coordinates which intrinsically trace the shoreline. Implicit finite-difference models for both sets of equations, as well as the nesting procedure, are explained briefly in § 2.3, while a more complete description is given in Appendix B. Readers who are interested in the runup results, while being less motivated for manipulation of long-wave equation and their numerical solution procedures, may skip § 2 as well as the appendix.

Testing is imperative since both sets of equations, as well as their numerical solution procedures, are new. In § 3, both the mathematical description of stationary wave patterns due to oblique incident waves and the numerical techniques are validated through comparison with existing results and models from the literature.

In § 4, simple estimates of runup heights for solitary waves of oblique incidence are suggested. Finally, computed runup heights are presented and discussed in the light of the estimates.

2. Basic theory, formulation

Our final goal is to compute the runup of solitary waves entering an inclined plane from a region of uniform depth at oblique angles of incidence. The first step is to adopt the transformation that Carrier & Noiseux (1983) employed for reflection of linear pulses, representing tsunamis. However, in our case, the transformation takes into consideration the nonlinear propagation speed of solitary waves and we wish to develop equations suitable for simulation of nonlinear and dispersive propagation, without any systematic degradation or loss of accuracy. For this purpose, the standard Boussinesq equations, in Eulerian coordinates, are subjected to the transformation and then further manipulated to enable subsequent computation of the solution in transects normal to beach, starting with the incident wave profile. However, dispersion is most pronounced in relatively large depths and the effect may be disregarded near-shore without noticeable influence on the runup height (see Pedersen 2008*b*, and § 3.2 herein). Thus, we derive specific equations for the near-shore region and inundation based on the nonlinear shallow-water theory. To achieve an automatic and accurate tracing of the shoreline, we describe these equations in Lagrangian coordinates which are related to streamlines in the stationary flow patterns.

Each of the models is solved by finite-difference techniques, which are described mainly in the Appendices. An operational model for runup, which is nonlinear everywhere and dispersive in finite depth, is then constructed by dynamic coupling of the Eulerian and the Lagrangian models.

A coordinate system with horizontal axes, $ox^\star$ and $oy^\star$, in the undisturbed water level and the vertical axis, $oz^\star$, pointing upwards is introduced. The asterisks indicate dimensional quantities, the fluid is confined to $-h^\star < z^\star < \eta^\star$ and the depth-averaged velocity is denoted by $\boldsymbol{v}^\star$. We introduce a characteristic depth d and dimensionless variables, according to

$$\left.\begin{aligned} &z^\star = \mathrm{d}z, && x^\star = \mathrm{d}x, && y^\star = \mathrm{d}y, \\ &t^\star = \mathrm{d}(gd)^{-1/2}t, && h^\star = \mathrm{d}h(x,y,t), && \eta^\star = \mathrm{d}\eta, \\ &\boldsymbol{v}^\star = (gd)^{1/2}\boldsymbol{v}, \end{aligned}\right\} \tag{2.1}$$

where g is the acceleration of gravity. The x- and y- components of $\boldsymbol{v}$ will be referred to as u and v, respectively. The scaling (2.1) is convenient for description of computational results as well as shallow-water equations. However, in derivation of long-wave equations, such as the Boussinesq equations, a scaling different from this is more useful and is even a *de facto* standard in the recent literature on dispersive long-wave equations. Introducing ϵ as a measure of nonlinearity and ℓ as a characteristic wavelength, dimensionless quantities are then defined as

$$\left.\begin{aligned} &x^\star = \ell\hat{x}, && y^\star = \ell\hat{y}, && t^\star = \ell(gd)^{-1/2}\hat{t}, \\ &\eta^\star = \epsilon d\hat{\eta}, && \boldsymbol{v}^\star = \epsilon(gd)^{1/2}\hat{\boldsymbol{v}}, \end{aligned}\right\} \tag{2.2}$$

while the dimensionless z and h are as in (2.1). Also, the non-dimensional wave celerity is the same in both scalings. It follows from (2.2) that the non-dimensional quantity $\mu^2 \equiv d^2/\ell^2$ indicates the importance of dispersion. The scaling (2.2) will be employed only in § 2.1 (with exception of figure 1) and § B.1, which are concerned with the derivation of Boussinesq equations and their numerical solution, respectively.

2.1. *Boussinesq equations and downstream marching*

From Peregrine (1972), we adopt the nonlinear and weakly dispersive Boussinesq equations on the standard form. Scaled according to (2.2), they read

$$\frac{\partial\hat{\eta}}{\partial\hat{t}} = -\hat{\nabla}\cdot((h+\epsilon\hat{\eta})\hat{\boldsymbol{v}}), \tag{2.3}$$

$$\frac{\partial\hat{\boldsymbol{v}}}{\partial\hat{t}} + \epsilon\hat{\boldsymbol{v}}\cdot\hat{\nabla}\hat{\boldsymbol{v}} = -\hat{\nabla}\hat{\eta} + \frac{\mu^2}{2}h\hat{\nabla}\hat{\nabla}\cdot\left(h\frac{\partial\hat{\boldsymbol{v}}}{\partial\hat{t}}\right) - \frac{\mu^2}{6}h^2\hat{\nabla}\hat{\nabla}\cdot\frac{\partial\hat{\boldsymbol{v}}}{\partial\hat{t}} + O(\mu^4, \mu^2\epsilon). \tag{2.4}$$

A number of Boussinesq formulations with improved dispersion properties and additional nonlinearities are available (Wei *et al.* 1995; Madsen & Schäffer 1999; Kennedy *et al.* 2000; Lynett *et al.* 2002). However, in the present study, we will combine nonlinear dispersive equations in finite depth with nonlinear shallow-water equations near the moving shoreline. Therefore, we stick to the standard equations even though some higher-order effects probably could be included in the following derivations.

We assume that the equilibrium shoreline and isolines for the depth are parallel to the $\hat{x}$-axis, implying that $h = h(\hat{y})$, and that a permanent form wave is incident from

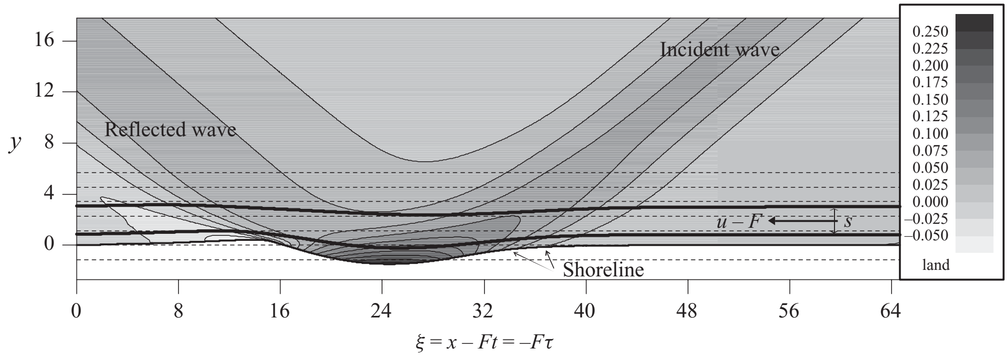

FIGURE 1. Diagram of the (ξ, y) plane with contours for the surface elevation corresponding to a stationary runup pattern of a wave incident from a region of constant depth. Depth contours, which are normal to the y-axis, are shown by dashed lines. In addition to the shoreline, two other streamlines, corresponding to arbitrarily selected a_1 and a_2, are shown by thick lines. If they are close the distance becomes $s \approx (\partial y/\partial a)(a_2 - a_1)$. Since the ξ-component of the velocity is $u - F$, the volume flux density (per a) between the streamlines becomes $(u - F)H(\partial y/\partial a)$. The diagram is intended as a definition sketch, but is based on the computed runup for a solitary wave for $A = 0.08$, $\phi = 10.54°$ and $\theta_i = 40°$ (see § 4.2). The increase in surface elevation before the crest enters the slope is due to interference with reflections of the wave front. The scaling (2.1) is used in this and all subsequent figures.

a region of constant depth, $h = 1$ (see figure 1). The wave pattern is then stationary in a frame of reference moving along the coast with the speed

$$F = c_i / \sin\theta_i, \tag{2.5}$$

where c_i and θ_i define the wave celerity and the direction of wave advance for the incident wave, respectively. Small values of θ_i, implying that we are close to normal incidence, correspond to high values of F. A new alongshore coordinate is defined as $\hat{\xi} = \hat{x} - F\hat{t}$. However, eventually, it is more convenient to work with the time-like variable $\hat{\tau} = \hat{t} - \hat{x}/F = -\hat{\xi}/F$. Substitution into (2.3) and (2.4) yields

$$\left.\begin{aligned}
&\hat{\eta}_{\hat{\tau}} - \epsilon F^{-1}(\hat{u}\hat{\eta})_{\hat{\tau}} + \epsilon(\hat{v}\hat{\eta})_{\hat{y}} = -(h\hat{v})_{\hat{y}} + F^{-1}h\hat{u}_{\hat{\tau}},\\
&\hat{u}_{\hat{\tau}} + \epsilon(-F^{-1}\hat{u}\hat{u}_{\hat{\tau}} + \hat{v}\hat{u}_{\hat{y}}) = F^{-1}\hat{\eta}_{\hat{\tau}} + \frac{\mu^2}{2}h(F^{-2}h\hat{u}_{\hat{\tau}\hat{\tau}\hat{\tau}} - F^{-1}(h\hat{v}_{\hat{\tau}\hat{\tau}})_{\hat{y}})\\
&\qquad - \frac{\mu^2}{6}h^2(F^{-2}\hat{u}_{\hat{\tau}\hat{\tau}\hat{\tau}} - F^{-1}\hat{v}_{\hat{\tau}\hat{\tau}\hat{y}}) + O(\mu^4, \mu^2\epsilon),\\
&\hat{v}_{\hat{\tau}} + \epsilon(-F^{-1}\hat{u}\hat{v}_{\hat{\tau}} + \hat{v}\hat{v}_{\hat{y}}) = -\hat{\eta}_{\hat{y}} - \frac{\mu^2}{2}h(F^{-1}(h\hat{u}_{\hat{\tau}\hat{\tau}})_{\hat{y}} - (h\hat{v}_{\hat{\tau}})_{\hat{y}\hat{y}})\\
&\qquad + \frac{\mu^2}{6}h^2(F^{-1}\hat{u}_{\hat{\tau}\hat{\tau}\hat{y}} - \hat{v}_{\hat{\tau}\hat{y}\hat{y}}) + O(\mu^4, \mu^2\epsilon),
\end{aligned}\right\} \tag{2.6}$$

where the indices correspond to partial differentiation. The number of dimensions is reduced by one. However, assuming that upstream influence is negligible, we seek equations that are suitable for forward integration in the time variable $\hat{\tau}$. To this end, we must remove the higher-order derivatives with respect to $\hat{\tau}$ in the dispersion terms.

In terms of the depth-averaged velocity components, the requirement of zero vertical vorticity reads as

$$\hat{u}_{\hat{y}} = \hat{v}_{\hat{x}} + O(\mu^2) = -F^{-1}\hat{v}_{\hat{\tau}} + O(\mu^2). \tag{2.7}$$

This relation is consistent with the momentum equation given in (2.6). However, the inclusion of bottom friction or wave breaking may produce vertical, in addition to horizontal, vorticity, which may be important for the near-shore flow regime (see Peregrine 1998; Bühler & Jacobson 2001; Brocchini *et al.* 2004). Hence, the presence of such effects would violate the relation (2.7) and the subsequent equations would have to be modified. The x-component of the momentum equation in (2.6) implies

$$\hat{u} = F^{-1}\hat{\eta} + C(\hat{y}) + O(\mu^2, \epsilon). \tag{2.8}$$

In the applications addressed herein, C may generally be set to zero. This is the case if, for instance, the medium is initially at equilibrium ($\hat{u} = \hat{\eta} = 0$). From (2.6), we then obtain the leading-order (in ϵ and μ) balance

$$(1 - hc_i^2F^{-2})\hat{u}_{\hat{\tau}\hat{\tau}} = -F^{-1}c_i^2(h\hat{v}_{\hat{\tau}})_{\hat{y}} + O(\mu^2, \epsilon) = c_i^2(h\hat{u}_{\hat{y}})_{\hat{y}} + O(\mu^2, \epsilon). \tag{2.9}$$

The phase speed, $c_i = 1 + O(\mu^2, \epsilon)$, of an incident wave in unitary depth is introduced to assure that the incident wave of permanent form fulfils (2.7) and (2.9) exactly. This is not strictly necessary, but it is convenient since the wave then remains an exact solution of our modified Boussinesq equations, regardless of the value of F. In the $\hat{x}$-component of the momentum equation, we first remove the $\hat{y}$-derivative in the convective term by means of (2.7). Then, the whole equation may be integrated in $\hat{\tau}$ to yield a Bernoulli equation, from which all remaining $\hat{\tau}$-derivatives are removed by (2.7) and (2.9). From the $\hat{y}$-component of the momentum equation, we eliminate $\hat{u}_{\hat{\tau}\hat{\tau}}$ with the aid of (2.9) and rewrite the convective terms by means of (2.7). Finally, we arrive at a set of nonlinear equations which appears somewhat complicated, but has a structure that is similar to that of the standard Boussinesq equations in time and one space dimension,

$$\hat{\eta}_{\hat{\tau}} - \epsilon F^{-1}(\hat{u}\hat{\eta})_{\hat{\tau}} + \epsilon(\hat{v}\hat{\eta})_{\hat{y}} = -(h\hat{v})_{\hat{y}} + F^{-1}h\hat{u}_{\hat{\tau}}, \tag{2.10}$$

$$\begin{aligned}\hat{u} - \frac{\epsilon}{2}F^{-1}(\hat{v}^2 + \hat{u}^2) = F^{-1}\hat{\eta} + \mu^2 h\left\{\frac{1}{3}h(F^2c_i^{-2} - h)^{-1} + \frac{1}{2}\right\}(h\hat{u}_{\hat{y}})_{\hat{y}}&\\ - \frac{1}{6}\mu^2h^2\hat{u}_{\hat{y}\hat{y}} + C(\hat{y}) + O(\mu^4, \mu^2\epsilon),&\end{aligned} \tag{2.11}$$

$$\begin{aligned}\hat{v}_{\hat{\tau}} + \frac{\epsilon}{2}(\hat{u}^2 + \hat{v}^2)_{\hat{y}} = -\hat{\eta}_{\hat{y}} &+ \frac{1}{2}\mu^2h(h\hat{v}_{\hat{\tau}})_{\hat{y}\hat{y}} - \frac{1}{6}\mu^2h^2\hat{v}_{\hat{\tau}\hat{y}\hat{y}}\\ &+ \frac{1}{3}\mu^2h^2\left\{\left(F^2c_i^{-2} - h\right)^{-1}(h\hat{v}_{\hat{\tau}})_{\hat{y}}\right\}_{\hat{y}},\\ &+ \frac{1}{2}\mu^2hh_{\hat{y}}\left(\left(F^2c_i^{-2} - h\right)^{-1}(h\hat{v}_{\hat{\tau}})_{\hat{y}} + O(\mu^4, \mu^2\epsilon),\right.\end{aligned} \tag{2.12}$$

where C is a temporal constant of integration that generally equals zero. The set is now in a form suitable for forward integration in $\hat{\tau}$ and will be used for simulation of the wave propagation in finite depth. During runup the equations may be used quite some distance onshore. There the dispersion terms are set to zero (see Appendix B.3).

When $\theta_i \to 0$, implying that $F \to \infty$, (2.11) gives $\hat{u} = 0$ while the other two equations are reduced to the ordinary Boussinesq equations in $\hat{y}$ and $\hat{t}$. Moreover, for large F (2.11) points to $\hat{u} = O(F^{-1})$ while the other field variables behave like $\hat{\eta}(\hat{y}, \hat{\tau}, F) = \hat{\eta}(\hat{y}, \hat{\tau}, 0) + O(F^{-2})$, $\hat{v}(\hat{y}, \hat{\tau}, F) = \hat{v}(\hat{y}, \hat{\tau}, 0) + O(F^{-2})$. Hence, to leading order the alongshore current may be obtained by first solving the equations for normal incidence, namely (2.10) and (2.12) without the terms containing $\hat{u}$ or reciprocals of F. Then $\hat{u}$ is found by substituting $\hat{\eta}$ and $\hat{v}$ into (2.11). A similar approach was used by Brocchini & Peregrine (1996) and Brocchini (1998), who obtained the normal incidence solution by applying the hodograph transformation to the NLSW ($\mu^2 \to 0$) counterparts to (2.10) and (2.12). In this approximation, (2.11) takes on the explicit form $\hat{u} = F^{-1}(\hat{\eta} + (1/2)\epsilon\hat{v}^2)$ (see Brocchini & Peregrine 1996, (2.19) and (2.15*c*) therein). In the study of weakly oblique bores, Ryrie (1983) employed a corresponding decoupling, by first solving for normal incidence and then obtaining the alongshore flow from the $\hat{x}$-component of the momentum equation, which was written in non-integrated form. Hence, no assumption of irrotational flow was required. However, to obtain a correction to the runup height, we must keep the coupling between $\hat{v}$, $\hat{\eta}$ and $\hat{u}$ in (2.10) through (2.12). Hence, in the numerical simulations, we retain all reciprocal orders of F, while the dispersion ($O(\mu^2)$) terms will be omitted near-shore (see § 2.2).

In Appendix A, limitations on the transformed equations are discussed in the light of so-called 'wave–waves' (described by, for instance, Miles 1977*b*). It is indicated in the appendix that the downstream-marching procedure is applicable for angles of incidence up to 60°, and even beyond this for small amplitudes.

2.2. *Use of Lagrangian streamline coordinates*

From this point, we employ the scaling (2.1). The Eulerian (y, τ) plane may be replaced by a pseudo-Lagrangian (a, τ) plane. The flow is stationary in the (ξ, y) plane, where $\xi = x - Ft$, and the Lagrangian coordinate, a, marks streamlines in this plane, rather than individual particles. In the Lagrangian equations, we will delete all dispersion terms (order μ^2 in the Boussinesq equations), but keep all nonlinearities in the hydrostatic parts of the equations.

It is convenient to first describe the streamline, or Lagrangian, coordinates in the (ξ, y) frame of reference. The velocity vector then becomes $(u - F)\boldsymbol{i} + v\boldsymbol{j}$, where $\boldsymbol{i}$ and $\boldsymbol{j}$ are the unit vectors in the x- and y-directions, respectively. A streamline is defined by $a(\xi, y) = \text{const.}$, which implies

$$(u - F)\frac{\partial a(\xi, y)}{\partial \xi} + v\frac{\partial a(\xi, y)}{\partial y} = 0, \quad \text{or} \quad \frac{\partial y(a, \xi)}{\partial \xi} = \frac{v}{u - F}. \tag{2.13}$$

When expressed in terms of τ, instead of ξ, these expressions take on the forms

$$\left(1 - \frac{u}{F}\right)\frac{\partial y(a, \tau)}{\partial \tau} = v, \tag{2.14}$$

$$\left(1 - \frac{u}{F}\right)\frac{\partial a(y, \tau)}{\partial \tau} + v\frac{\partial a(y, \tau)}{\partial y} = 0. \tag{2.15}$$

For the material derivative of some quantity, G, we obtain the expression

$$\frac{\mathrm{D}G}{\mathrm{D}t} = \left(\frac{\partial}{\partial t} + u\frac{\partial}{\partial x} + v\frac{\partial}{\partial y}\right)G(x, y, t) = \left(1 - \frac{u}{F}\right)\frac{\partial G(a, \tau)}{\partial \tau}. \tag{2.16}$$

Naturally, (2.14) is only an instance of (2.16) with $G = y$.

The continuity equation (2.10) can be transformed by the introduction of the total fluid depth, $H = \eta + h(y)$, the spatial variable a instead of y, and finally by application of (2.16). Important cancellations occur to yield a separable equation for H, u and $\partial y/\partial a$, which may be integrated in τ. We omit the details and present the transformed continuity equations as

$$\left(1 - \frac{u}{F}\right)H\frac{\partial y}{\partial a} = K(a), \tag{2.17}$$

where K is a constant of integration which is determined by the initial conditions. A simple interpretation of the first integral (2.17) is that the volume flux between two adjacent streamlines in the (ξ, y) plane is constant (see figure 1). The first factor on the left-hand side of (2.17) is proportional to the current, while the second and third factors are the height and relative horizontal extension of the fluid cross-section, respectively. When $F \to \infty$, (2.17) simplifies to express conservation of volume in material columns moving normal to the x-axis as u/F vanishes and the flux in the x-direction can be regarded as independent of y.

When the dispersion ($O(\mu^2)$) terms are omitted the x-component of the momentum equation (2.11) becomes a purely algebraic equation which is unaltered during the transformation to Lagrangian coordinates. For the y-component, we better start with the form in (2.6). Using (2.16) and rewriting the surface elevation gradient, as done by Jensen *et al.* (2003), we then readily find

$$u - \tfrac{1}{2}F^{-1}(v^2 + u^2) = F^{-1}\eta, \tag{2.18}$$

$$\left(1 - \frac{u}{F}\right)\frac{\partial v}{\partial \tau} = -\left(1 - \frac{u}{F}\right)\frac{H}{K}\frac{\partial H}{\partial a} + \frac{\mathrm{d}h}{\mathrm{d}y}. \tag{2.19}$$

The set (2.14), (2.17), (2.18) and (2.19) will be solved numerically in the near-shore region.

The most important consequence of the transformation to Lagrangian coordinates is that the shoreline, which is a streamline in the (ξ, y) plane, is associated with a constant a, namely $a = 0$ in the cases studied herein.

2.3. *Numerical methods and incident waves*

The set of Eulerian equations (2.10), (2.11) and (2.12) is solved in finite depth by a method related to that described by Løvholt, Pedersen & Gisler (2008) and references therein. In the vicinity of the shoreline the Lagrangian equations, (2.14), (2.17), (2.18) and (2.19), are solved by a generalization of the technique employed by Jensen *et al.* (2003) and tested by Pedersen (2008*a*). In both cases, finite differences on staggered grids lead to implicit equations at each time step, which are solved by iteration. The resulting combined model is nonlinear throughout and dispersive in finite depth.

The near-shore Lagrangian grid is combined with a finite-depth Eulerian grid through a suitable overlap and the total solution is obtained by Schwartz iteration at each time step. Initially, the Lagrangian grid extends from the beach ($a = 0$; $y = 0$ at equilibrium) to $y = a = a_L$ and the Eulerian grid starts at $y = y_E < a_L$. During the simulation, new nodes are included or exempted from the computational Eulerian grid to keep the extent of the overlap of roughly the same size. The temporal discretizations ($\Delta\tau$) in the two grids are identical, while the spatial resolutions, Δa and Δy respectively, will differ.

Details on the numerical procedure are given in Appendix B. All reported solutions are subjected to grid-refinement tests. Also, the sensitivity with respect to other parameters, such as the width of the overlap, is investigated. In addition to the nonlinear model outlined above, we will also employ a linear, non-dispersive model for comparison (see § B.4).

As incident waves we employ solitary waves that are specified in regions of unitary dimensionless depth. Because of the particular choice for the dispersion terms, (2.10) and (2.11) share the solitary wave solution with (2.3) and (2.4), as well as the

Boussinesq formulations used by Pedersen (1988, 1996):

$$\eta = Y(\cos\theta_i y + c_i\tau), \quad u = \sin\theta_i U(\cos\theta_i y + c_i\tau), \quad v = -\cos\theta_i U(\cos\theta_i y + c_i\tau), \tag{2.20}$$

where Y and U are shape functions. For vanishing A, the above solution approaches the standard solitary wave solution given in § 3.2, but we invoke the full solutions of our Boussinesq-type equations in the simulations. The use of the solitary wave as an initial condition in the Eulerian model is straightforward, but to avoid first order discretization errors the initial v must be shifted $(1/2)\Delta\tau$ relative to η and u, due to the staggered grid (see Appendix B). The height of the solitary wave decays exponentially as $|\cos\theta_i y + c_i\tau| \to \infty$. In the initial conditions, the profiles are truncated when $\eta/A < e_t$, where $e_t = 0.0002$ in general.

A moving shoreline may be contained in the Lagrangian part of the model and the condition $H = 0$ (zero flow depth) is invoked there. At the offshore boundary, a no-flux condition is used. This will suffice because the incident wave is unidirectional (onshore) and the deep region is large enough to avoid the influence of reflections from the deep water wall on the runup.

3. Assessment and validation of method

In our approach there are two features, in particular, that call for verification.

Firstly, the transformed description of the nonlinear, oblique wave pattern, as given by the equation set (2.10)–(2.12) should be controlled as such. This set is not limited to runup on sloping beaches. Hence, in § 3.1 we compare our Eulerian model with an existing Boussinesq model, from the literature, for refraction from a shelf and reflection from a vertical wall. This test involves neither runup on sloping beaches nor Lagrangian coordinates. In addition, our Eulerian (with the dispersion terms omitted) and Lagrangian models were compared for oblique waves in finite depth (results not shown).

Secondly, we need to verify the numerical implementations and, above all, their coupling. To this end, we simulate runup of solitary waves of normal incidence and compare with results from the literature in § 3.2. In this section, we also include some general properties of solitary wave runup which are useful elsewhere in this article. We have also verified the numerics employing the standard problem of runup of an N-wave on an inclined plane as described by Carrier *et al.* (2003) and Liu *et al.* (2008) (results not shown).

All tests have been passed successfully.

3.1. *Refraction at a shelf and reflection from a vertical wall*

Normal and abnormal refraction patterns on slopes were computed by a 2HD (two horizontal dimensions and time) Boussinesq-type model by Pedersen (1996). Later, it has come to light that this and most other Boussinesq models, except the standard formulation, are prone to instabilities due to steep bottom gradients (Løvholt & Pedersen 2008). Still, for the gentle slopes and the wave patterns that were investigated by Pedersen (1996), as well as the one in this subsection, no instabilities have been observed. The incident solitary wave is specified in a region of unitary dimensionless depth. From this region, a linear slope of width 25 length units leads up to a shelf of depth 0.5 and width 25 (see figure 2). The shelf is terminated by a vertical wall and there is no sloping beach in the geometry. Hence, the incident wave is first refracted at the slope. The shape, which is no longer that of a single solitary wave, then modifies due to nonlinear and dispersive effects during the propagation (back and forth)

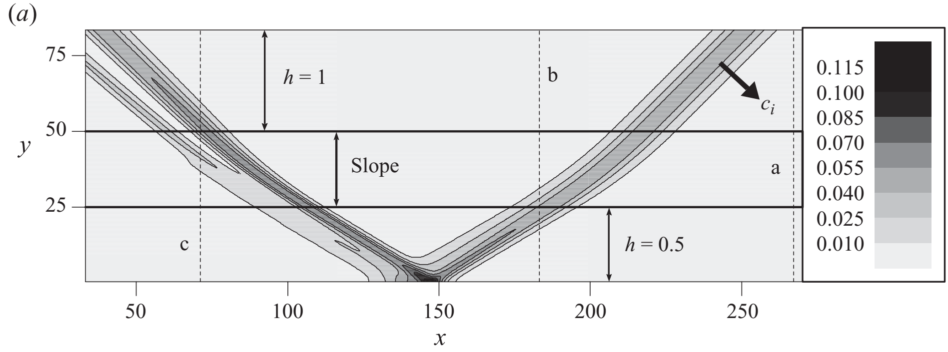

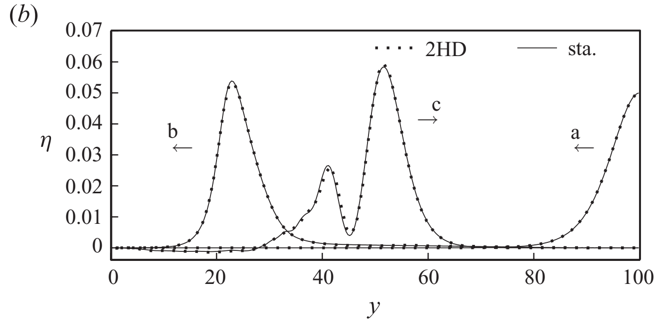

FIGURE 2. Stationary wave pattern for a solitary wave of amplitude $A = 0.05$ and angle $\theta_i = 45°$, encountering a shelf and a vertical wall. (*a*) Contour diagram for η from the 2HD simulation. The dashed transects correspond to the profiles shown in (*b*). Only a part of the computational domain is displayed. (*b*) Comparison of the 2HD simulation with a corresponding simulation based on the mathematically one-dimensional formulation used herein (sta.). Profiles are shown for three different stages: the incident wave (a), an instant when the crest enters the shelf (b) and after the wave has been reflected from the wall and the leading crest has descended the slope again (c).

over the shelf and reflection from the wall. Thereafter, the wave is again refracted during the descent of the slope towards deeper water. In the 2HD simulation, the incident wave is specified as a moving input boundary condition, while a radiation condition is employed for the reflected wave. For the incident wave, we choose the parameters $A = 0.05$ and $\theta_i = 45°$. In the 2HD model, a grid increment $\Delta x = \Delta y = 0.25$ is employed, which, according to grid-refinement tests, yields a general error much less than 1 %. For the marching technique we employ a similar resolution as in § 4.2. The wave pattern, as obtained from the 2HD model, and the comparison are shown in figure 2. The agreement between the models is very close, even for the last stage shown, where the wave has descended the slope again while undergoing fission into two distinct crests.

3.2. *Runup of solitary waves of normal incidence*

Synolakis (1987) derived a closed-form asymptotic expression for the runup of solitary waves incident from a region of constant depth on a plane beach with inclination angle ϕ. The incident pulse was specified according to

$$\eta = A\,\mathrm{sech}^2(k(y - ct)), \tag{3.1}$$

where the y-axis is normal to the shore, the dimensionless maximum depth equals unity and

$$k = \tfrac{1}{2}(3A)^{1/2}. \tag{3.2}$$

The combination of (3.1) and (3.2) describes the leading-order approximation to a solitary wave, as obtained by solving the Korteweg-de Vries (KdV) equation. It is remarked that this is slightly different from the solitary wave solution of our Boussinesq equations. Synolakis' solution reads as

$$R_S(A) = AK_S(\cot\phi)^{1/2}(A)^{1/4}, \quad \text{for} \quad \sqrt{A}\cot\phi \to \infty,\ A \to 0, \tag{3.3}$$

where $K_s = 2.831$ is a numeric constant. This formula also applies to weakly oblique cases as described by Brocchini (1998). In the derivation of (3.3) in Synolakis (1987) the relation (3.2) is invoked only at the very last stage. Hence, the derivation inherits the runup solution for a two-parameter class of pulses, where A and k are independent, rather than being restrained by (3.2). This is due to the fact, pointed out in the reference, that the relation between the incident wave and the maximum runup is linear, even though the solution behaves nonlinearly elsewhere (see also Didenkulova 2008). The more general formula for independent k and A, which will be used in §4.1, reads as

$$R_P(A,k) = A\frac{2^{1/2}K_S}{3^{1/4}}(k\cot\phi)^{1/2}, \quad \text{for} \quad k\cot\phi \to \infty,\ A \to 0. \tag{3.4}$$

We observe that R_P/A depends solely on the quantity $k\cot\phi$, which is proportional to the length of the slope relative to the length of the incident wave.

Pedersen (2008*b*) compared (3.3) with simulations based on the Serre equation (full nonlinearity, standard Boussinesq dispersion) discretized on a single Lagrangian grid. In Pedersen (2008*b*), computations were also made with the NLSW equations and a variable dispersion according to putting $\mu(a)$ in the Serre equations, where μ was reduced continuously from its proper value to zero between $a = 1.1a_c$ and $a = a_c$. In that context, μ had the same role as in the Boussinesq equations of §2.1. Hence, the region $a < a_c$ was treated with the NLSW equations. This is analogous to the present combination of Boussinesq and NLSW equations, with a_L (see §2.3) comparable to a_c.

In figure 3, we compare runup heights from the present combined Eulerian/Lagrangian model with those from (3.3) and numerical simulations of both Serre and the NLSW equations from Pedersen (2008*b*). The deviations between the latter three data sets are discussed by Pedersen (2008*b*). The present model, with $a_L = 0.1\cot\phi$, $y_E = 0.05\cot\phi$ and a resolution similar to that used in figure 5, and the Serre model agree very well, with the present model yielding slightly higher R. It is noteworthy that the differences between the Serre results for $a_c = 0$ and $a_c = (1/4)\cot\phi > a_L$, respectively, are even smaller. This indicates that the small deviations between the present model and that of Pedersen (2008*b*) stem from differences in the solitary wave shape and deep water propagation properties, rather than the omission of dispersive effects near-shore in the combined model used herein.

The models employed herein are limited to non-breaking waves. For solitary waves on an inclined plane, Synolakis (1987) reported a breaking criterion based on nonlinear shallow-water theory

$$A = 0.818(\tan\theta)^{10/9}. \tag{3.5}$$

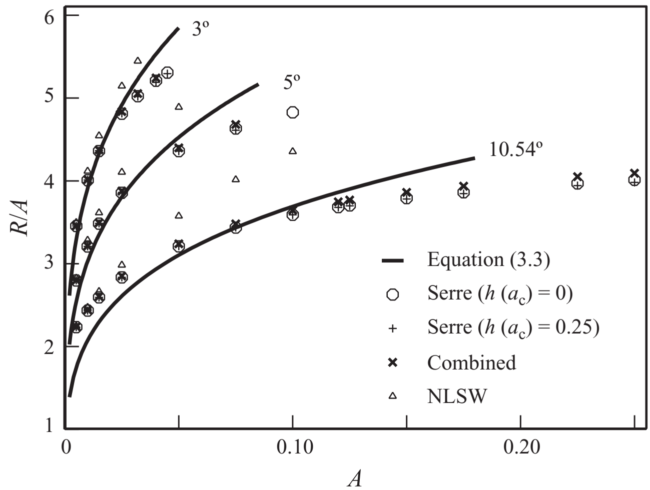

FIGURE 3. Maximum runup heights for solitary waves. Results from the present, combined Eulerian/Lagrangian model are denoted by 'combined'. As explained in the text, the quantity a_c indicates the extent of the near-shore region where the dispersion term is turned off in the Serre simulations. The value $h(a_c)=0$ implies that the Serre equation is used all the way to the instantaneous shoreline.

For high, and thereby short, incident solitary waves, dispersion during shoaling is important and (3.5) becomes inadequate. On the basis of simulations with a boundary-integral technique and curve fitting, Grilli, Svendsen & Subramanya (1997) reported

$$A = 25.7(\tan\theta)^2, \tag{3.6}$$

as a criterion for breaking during runup. For large θ, this criterion is much more relaxed than (3.5). For $\theta=10°$, for instance, (3.6) and (3.5) yield $A=0.52$ and $A=0.12$, respectively. For smaller θ, the difference is less pronounced. No criteria are available for oblique solitary waves. Anyhow, all incident waves employed herein have amplitudes well below the limitation (3.6) for normal incidence.

4. Oblique runup of solitary waves

We investigate the runup of solitary waves incident on a plane beach, with inclination angle ϕ, from a region of constant depth which equals unity in dimensionless coordinates. An illustration of a typical runup wave pattern is given in figure 1.

For the runup of solitary waves on an inclined plane, there are no known rigorous analytic solutions, in the sense that they include the variation of the runup height with the angle of incidence. However, heuristic estimates can be provided by combining optical descriptions and the solution (3.4).

4.1. *Simple estimates of maximum runup*

If the slope is sufficiently gentle the incident wave will maintain its identity as a solitary wave with approximately the same dependence of shape and wave celerity on amplitude and local depth as if in uniform medium. To leading order, the shoaling will produce a single crested wave with amplification and refraction according to

(Miles 1977*a*; Pedersen 1996)

$$\cot\theta\, E(\alpha, h) = \text{const.}, \qquad \frac{c}{\sin\theta} = F, \tag{4.1}$$

where $\alpha(y)$ is the local amplitude to depth ratio, $\theta(y)$ defines the local direction of wave advance, $E = 8(h\alpha/3)^{3/2}$ is the leading-order (in α) energy per crest length of a solitary wave and $c = h^{1/2}(1 + (\alpha/2h))$ is the leading-order local wave celerity. These equations express that the onshore energy flux is constant and that the crest is stationary (in the (ξ, y) plane), respectively. At $h = 1$, the incident wave is specified according to $\alpha = A$ and $\theta = \theta_i$.

According to (4.1) the angle θ will decrease towards zero as we approach the shoreline. We may then assume that the runup will correspond to a case of normal incidence where the wave height at $h \to 0$ matches that for our case of oblique incidence. It follows from (4.1) that the amplitude, A_N, of an equivalent case of normal incidence is determined by $E(A)\cos\theta_i = E(A_N)$, meaning $A_N = A\cos^{2/3}\theta_i$. Employing (3.3), we then find the runup estimate

$$R(A, \theta_i) = R_S(A_N) = R_S(A)\left(1 - \frac{5}{12}\theta_i^2 + \cdots\right) = R_S(A)\left(1 - \frac{5}{12}F^{-2} + \cdots\right), \tag{4.2}$$

where relative error terms, proportional to θ_i^4, F^{-4} and A, are implicit in the expressions. Several objections can be raised against this estimate. Firstly, the slope must be very gentle for solitary wave optics to apply. It is not sufficient that the slope length is large compared to the wavelength; the slope length must be large in comparison with the much longer scales linked to the evolution of dispersive and nonlinear effects (Miles 1980; Pedersen 1996). This is not properly fulfilled for the runup computations of non-breaking waves that will be presented subsequently. Secondly, solitary wave optics, like all kinds of optics, will be invalid close to the shoreline where it predicts $A \to \infty$. Moreover, our arguments behind (4.2) require that the wave is close to normal incidence near-shore, which implies $u \ll v$. According to (2.11), u does not go to zero as the beach is approached and for small F and long incident waves u may not be small in comparison to v. However, the use of (4.2) means that we relate the runup of an oblique wave to that of a wave of normal incidence, with the same onshore energy transport per length of the shoreline. This might still provide a sensible estimate of the effect of obliqueness.

In contrast to the solitary wave case, the optical approximation is often quite good for linear waves, even if the length scale of the geometry does not exceed the wavelength by an order of magnitude. Assuming that the slope length is too short for dispersive effects to be important and that nonlinear effects are crucial only near-shore, we may use linear, non-dispersive optics. The above application of (4.1) is then repeated, but with $c = h^{1/2}$ and the energy density replaced by $E = E_k\alpha^2/k$, where E_k is a constant. Here k is the pulse wavenumber as used in (3.1). For the incident wave only, we have $k = (1/2)(3A)^{1/2}$. In agreement with the kinematic condition, the time scale of the pulse is constant, implying that $kh^{1/2}$ is constant. For normal incidence, this yields Green's law for the amplitude, while the match of near-shore behaviour now implies $A_N = A\cos^{1/2}\theta_i$ and (3.4) gives

$$R(A, \theta_i) = R_S(A)\left(1 - \frac{5}{16}\theta_i^2 + O\left(\theta_i^4\right)\right), \tag{4.3}$$

which yields a smaller reduction in R due to obliqueness than does (4.2).

The main shortcoming of the estimate (4.3) is the absence of nonlinear effects. When dispersive effects are assumed to be less significant during shoaling, steepening of the wavefront becomes an important nonlinear effect, resulting in an asymmetric wave. For non-breaking waves, this increases the runup heights (see, for instance, Didenkulova *et al.* 2007). Steepening depends on the amplitude and the propagation distance available for its evolution. The effect of the latter surfaces in (3.4) through the factor $k\cot\phi$, which measures propagation distance relative to wavelength. In the case of oblique incidence, the propagation distance is increased. This again points to an extra steepening of the front compared with the equivalent wave (same amplitude near-shore) of normal incidence. An indication of the increased runup due to this effect may be obtained by replacing the factor $\cot\phi$ by the arclength ℓ of the ray in (3.4). Employing the linear version of the kinematic condition, we find

$$\ell = \int_0^{\cot\phi} \frac{\mathrm{d}y}{\cos\theta} = \frac{2\cot\phi}{1+(1-F^{-2})^{1/2}}. \tag{4.4}$$

Expanding this to the two leading orders in F^{-2} and inserting the result for $\cot\phi$ into (3.4) we obtain a correction factor $(1+\theta_i^2/8)$ which in combination with (4.3) yields

$$R(A,\theta_i) = R_S(A)\left(1-\frac{3}{16}\theta_i^2+\cdots\right). \tag{4.5}$$

The evolution of the wave height during the initial stages of the shoaling may give a clue concerning which ray theory is the more appropriate. Linear ray theory predicts amplification when $\theta < 45^\circ$ and attenuation for $\theta > 45^\circ$. The corresponding limit for solitary wave optics is $\theta = 60^\circ$ when $A \to 0$ (see Pedersen 1996, figure 1; observe the different definition of θ). Computed wave heights (not shown) display no attenuation for the smallest A, for which any kind of optics is inappropriate since the wavelength is much longer than the inclined plane, and a shift from amplification to attenuation somewhat above $\theta_i = 55^\circ$. Bearing in mind that interference with the reflected wave is bound to shift this transition upwards, we may interpret this as an intermediate behaviour in relation to the optical predictions.

In general, we may write the runup height for an oblique solitary wave as $R(A,\phi,F^{-2})$. For large F (close to normal incidence), the above analysis suggests

$$\gamma(A,\phi) = \frac{1}{R(A,\phi,0)}\frac{\partial R(A,\phi,0)}{\partial(F^{-2})}, \tag{4.6}$$

as a useful quantity for further investigation. The estimates may be then summarized as follows:

$$\gamma = \begin{cases} \gamma_s = -\dfrac{5}{12} & (4.2), \\[2mm] \gamma_l = -\dfrac{5}{16} & (4.3), \\[2mm] \gamma_n = -\dfrac{3}{16} & (4.5). \end{cases} \tag{4.7}$$

It is emphasized that these values of γ should not be regarded as rigorous mathematical results. Still, as shown later, they envelop most of the numerical results in a nice manner.

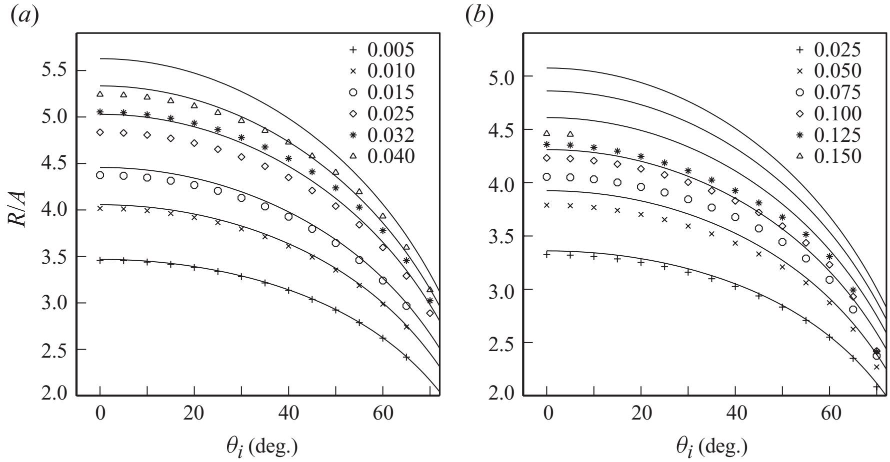

FIGURE 4. Runup heights as functions of the angle of incidence, θ_i, for different values of A as indicated by the labels. Symbols correspond to the combined Eularian/Lagrangian model, while the lines represent linear, hydrostatic computations. The correct match between symbols and curves are found by counting from below (or from the top). (*a*) $\phi = 3°$ and (*b*) $\phi = 7.18°$.

4.2. *Computations*

Simulations have been performed with a junction in the depth function, which is either a vertex or a smoothed bend which extends one tenth of the equilibrium beach length and is represented by a polynomial that assures continuous second derivatives of h. For the vertex the solution of our Boussinesq-type model has a faint local distortion, which is often hard to notice. In the simulation in figure 2, for example, apices are present both at $y = 25$ and at $y = 50$, but the distortion cannot be discerned. The smooth transition yields runup heights that are slightly higher than for the vertex. For the steepest inclination, $\phi = 10.54°$, the relative difference is less than 10^{-4} for $A = 0.05$ and $\theta_i = 0°$ and increases to nearly 10^{-3} for $A = 0.175$ and $\theta_i = 65°$. Generally, the relative difference is comparable to, or smaller, than the discretization errors (around 0.001, see below). In the following, the smooth bottom is employed in the computations. Likewise, the variation of the truncation limit (see § 2.3) indicates that $e_t = 0.0002$ also yield smaller errors than the finite resolution.

Computations are reported for $\phi = 3°$, $5°$, $7.18°$, $10.54°$, covering a large span of amplitudes and grid resolutions for each inclination. The simulations are performed with a Lagrangian near-shore grid that initially extends to $y = a_L = (1/10)\cot\phi$, which is one tenth of the equilibrium slope length. The overlap with the Eulerian grid is kept roughly constant according to $y_E = (1/20)\cot\phi$. Moderate variations of the overlap and the size of the Lagrangian grid have minor effect on the runup heights. However, the inclusion of new Eulerian grid points at the beach during runup implies stepwise changes in the length of the overlap. Because there are differences, even if small, in the properties of the models in the overlap, this will result in small fluctuations in the solutions. Hence, grid-refinement tests are important. Grid effects are included in figure 5.

Runup heights for two selected inclination angles are shown in figure 4. A decrease of R/A with the angle of incidence, θ_i, is observed. This decrease becomes stronger for the larger amplitudes, causing the curves for different amplitudes to nearly collapse for $\theta_i > 65°$, say. A similar trend is also observed for the other inclination angles (not

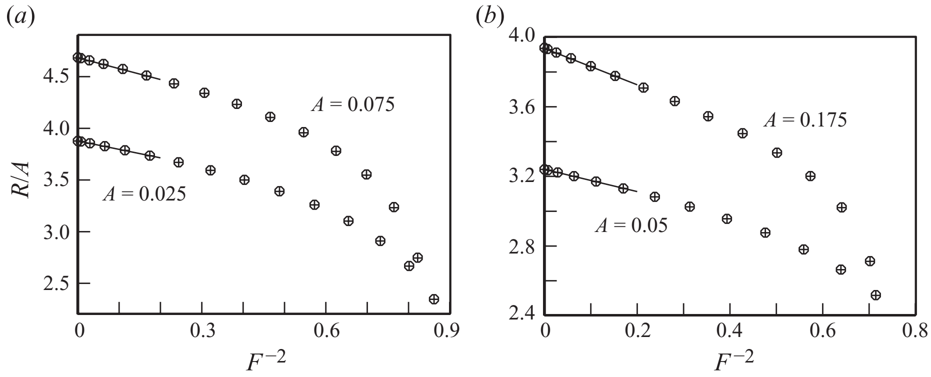

FIGURE 5. Runup height as a function of F^{-2} for selected values of A. Computed results with finest resolution are shown by + symbols, while circles (○) correspond to half this resolution and fully drawn lines are the best linear fit which determine the factor γ. (*a*) $\phi = 5°$, $\Delta y = 0.0351$, $\Delta a = 0.0164$; (*b*) $\phi = 10.54°$, $\Delta y = 0.0238$, $\Delta a = 0.0085$, where the grid increments correspond to $\theta_i = 45°$ and the highest amplitude.

shown). The figure also includes runup heights from linear hydrostatic computations (see § B.4). The comparison of linear results with the nonlinear computations is motivated by the good performance of linear theory observed for normal incidence (see, for instance, Didenkulova 2008, and the discussion before (3.4) herein). For the smaller amplitudes, the agreement between these and the nonlinear, dispersive results is close, and even for the higher amplitudes the discrepancy does not exceed 15 %. As θ_i increases, the difference between nonlinear and linear runup heights diminishes somewhat. This indicates that the unexpectedly good performance of linear runup models carries over to the oblique case as well. On the other hand, it is not surprising that linear theory performs better for larger ϕ, where the runup heights and wave heights during shoaling are relatively smaller.

The relative rate of decrease of the runup height with obliqueness, as represented by γ defined in (4.6), is extracted from the computations. For small F^{-2}, we use linear regression on R for each A and ϕ. The regression interval and the resulting best linear fit are shown in figure 5 for selected amplitudes and slopes. Results obtained with half the number of grid points are also included. The typical relative differences of about 0.001, or less, are scarcely visible in the figure. The linear regression displayed in figure 5 is very good and should provide accurate values for γ. Moreover, the decrease rate with F^{-2} does not change much until $F^{-2} = 0.5$, say, which roughly corresponds to $\theta_i = 45°$. For larger angles of incidence the reduction rate for R becomes markedly larger.

In figure 6, the computed values of γ have been summarized and compared with the three optical estimates from § 4.1. For the smallest amplitude, the incident solitary waves are long in comparison with the slope length ($\cot\phi$). Then, ray theory does not apply. In the limit $A \to 0$, the beach will act as a vertical impermeable wall and $R/A \to 2^+$ regardless of the angle of incidence θ_i, which in turn implies $\gamma \to 0^-$. For moderate values of A, the factor γ falls between γ_n and γ_l. It is not surprising that γ_n is an overestimation since it includes enhancement of nonlinear effects due to the prolonged arclength of the ray (as compared with that of normal incidence), while counteracting dispersive effects are neglected. For the three larger inclination angles the effect of obliqueness increases slowly with A and we may finally obtain values below γ_l. However, we have not observed computed γ values close to γ_s.

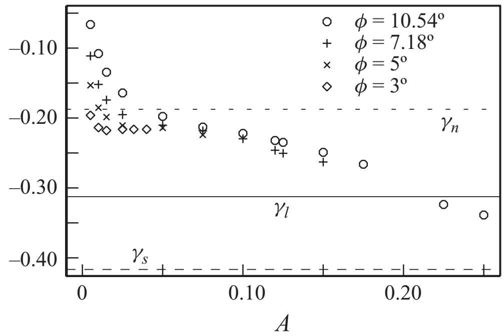

FIGURE 6. The factor γ as defined in the text.

5. Concluding remarks

Under the assumption of stationary wave patterns in a moving frame of reference, nonlinear long-wave equations were transformed into a form allowing downstream marching, where one coordinate direction is traversed by forward integration in a time-like variable. The structure of the marching equations was made quite similar to that used for propagation in one horizontal dimension, even when weak dispersion, corresponding to the standard Boussinesq equations, was included. No attempt has been made to do a similar transformation for higher-order Boussinesq-type equations and it is open whether or not this would provide a useful basis for numerical simulations. For the nonlinear shallow-water part of the marching equations, Lagrangian, or rather streamline, coordinates could be employed to derive a description that inherently traces the shoreline.

A refraction problem was used to demonstrate both the applicability of the marching approach and its numerical realization. For this problem, the wave pattern computed by a Boussinesq model with two horizontal dimensions was reproduced with great accuracy. The combination of an Eulerian Boussinesq model for finite depth and Lagrangian (streamline) model for the vicinity of the shoreline was tested on cases with normal incidence and through grid refinement. This is not the main issue herein, but it is noteworthy that the dynamic coupling of the static Eulerian grid and the small, rapidly moving, Lagrangian grid worked that well. Naturally, new problems may be encountered if a similar approach was attempted in more general cases.

The reduction of runup heights due to obliqueness is, as can be expected, very small for the combination of long incident waves and steep beaches. For moderate angles of incidence, we may write $R(A, \phi, \theta_i) \approx R(A, \phi, 0)(1 + \gamma\theta_i^2)$, where A, ϕ and θ_i are amplitude, slope inclination and angle of incidence, respectively. Alternatively, θ_i on the right-hand side may be replaced by $1/F = \sin\theta_i/c_i$, where F is the speed of the frame of reference in which the wave pattern is stationary. Except for very long incident waves, typical computed γ values are in the range -0.2 to -0.37, say. This compares well with the three estimates inspired by optics, namely $\gamma = -0.19, -0.31$ and -0.42. Moreover, the reduction rate of R with $1/F^2$ does not change dramatically for $\theta_i < 45°$. A typical value $\gamma = -0.25$ and an angle of incidence $\theta_i = 45°$ then yield a reduction of R of approximately 12 % as compared to the case of normal incidence. For larger angles of incidence, the reduction rate increases somewhat.

It is well known that linear shallow-water theory may perform surprisingly well for runup of waves of normal incidence. Our results suggest that this theory is at least as good for moderate obliqueness, with angles of incidence up to 70°, say.

The present investigation has been limited to waves that do not break during runup, even though the higher amplitude cases will break during drawdown. Breaking may be introduced in the fashion of Kennedy *et al.* (2000), for instance. If the dispersive terms are omitted, more options are available. However, breaking will introduce rotation and a reformulation of the equations used herein would be required.

Appendix A. Validity of downstream marching

In Pedersen (1988), a marching procedure similar to the present one gave very good agreement with simulations by a more general model, involving evolution in two horizontal dimensions and time, for supercritical wave generation by a pressure disturbance in a channel. As expected, the marching procedure failed when the Froude number came close to the trans-critical regime with upstream emission of waves. According to Pedersen (1988), the upper limit of the trans-critical regime is linked to the speed of 'wave–waves' in the form of nonlinear modulations on solitary waves (Reutov 1976; Miles 1977*a*; Ko & Kuehl 1979; Pedersen 1994). The modulations may propagate, in both directions, along a solitary carrier wave with speed $\pm c_m$. For gentle modulations and small carrier-wave amplitudes (A), the speed is $c_m = ((1/3)A)^{1/2}$. To prevent modulations from travelling upstream in our stationary pattern, we must then require

$$\sqrt{\frac{A}{3}} \approx c_m < c \cot\theta \sim \sqrt{h}\left(1 + O\left(\frac{A}{h}\right)\right)\cot\theta, \tag{A 1}$$

where A and θ are the local amplitude and the angle of incidence of a solitary-wave crest, respectively.

While the criterion (A 1) assures that infinitesimal modulations on a solitary crest do not propagate upstream, it does not apply to configurations where wave jumps, in the sense of strong and abrupt variation of wave characteristics along a crest (Miles 1977*a*; Peregrine 1983; Pedersen 1994), are involved. An example of such a process is Mach reflection from a straight wall in constant depth, which occurs when $\sqrt{3A} > (1 + O((A/h), \theta_i^2))\sqrt{h}((\pi/2) - \theta_i)$ (see Miles 1977*b*, *c*). Clearly, this phenomenon is outside of the validity range of our marching procedure, thus imposing a stronger constraint than (A 1). Still, to leading order in A and $(\pi/2) - \theta$ both requirements are of the form

$$\left(\frac{A}{h}\right)^{1/2} < C\left(\frac{\pi}{2} - \theta\right). \tag{A 2}$$

There is no reason to expect formation of wave jumps during runup, unless the slope is very steep. Hence, we may employ (A 1). For $\theta_i = 60^\circ$, this criterion yields $A < 1$, which includes much more than the meaningful range of solitary wave amplitudes. For $\theta_i = 75^\circ$ and $\theta_i = 80^\circ$, we find $A < 0.21$ and $A < 0.09$, respectively, which still leave an appreciable amplitude range. The question then is whether or not the criterion (A 1) may be violated during shoaling.

Ray theory may also be applied to investigate if the criterion (A 1) may be violated during shoaling, even when it is fulfilled for the incident wave. Assuming that the wave remains of solitary shape, one finds that the critical relation is approached when θ_i is somewhat larger than 45° or when $h \to 0$, when the ray theory in any case is dubious. On the other hand, when the linear non-dispersive ray theory is employed, we always move away from the limit of (A 1) during shoaling. Unfortunately, since the true behaviour falls between the different ray theories (see § 4.1), their application yields no clear indication whether or not the criterion (A 1) becomes more critical as the depth decreases.

Naturally, a criterion such as (A 1) is only a necessary condition for applicability of our theory. The possibility that there are other causes for limitations on the validity range cannot be excluded. Experience with the simulations reported in § 4.2 suggests that the applicability of the marching procedure is somewhat more restricted than indicated by the above criterion. For a given A, the solution breaks down for θ_i that is 5°–10° smaller than that predicted by (A 1). For instance, the parameters $A = 0.15$, $\theta_i = 70°$ and $\phi = 10.54°$ lead to an apparent instability in the incident wave that rapidly stops the simulation. The evolution of this instability seems independent of the resolution as well as the number of iterations in the numerical method. Even if there is no breakdown in the incident wave or during shoaling, we have no guarantee that the results obtained for the largest values of θ_i are quantitatively accurate. Hence, we report computed runup heights when reasonable values have been obtained, but the most oblique cases should be taken critically.

Appendix B. Numerical methods

In the following, we use the notations δ_q and $\overline{()}^q$ for the centred, divided difference and the average, respectively, with regard to the variable q. These operators involve two neighbouring points and give discrete approximations to the first partial derivative and the function itself, respectively. The grid site of a quantity is specified by a subscript for the spatial location and a superscript for the time. The difference and the average then inherit indices which are shifted by a half relative to that of the quantity itself. When all discretization, as far as possible, are based on midpoint representations, the different terms of a difference equation usually end up with identical indices which correspond to the 'simulation node' of the equation. This is exploited by collecting the terms within square brackets, while leaving the indices outside. Details on the notation can be found in, for instance, Pedersen (1988). Either the subscript or superscript on discrete quantities or equations may be omitted. The implicit index is then arbitrary or the value can be inferred from the context.

B.1. *Eulerian marching procedure*

In this subsection, we describe the finite-difference method for the equations derived in § 2.1. In that section we employ the scaling (2.2), but this time we omit the hats (ˆ). We regard τ as a time variable and discretize the equations on a staggered grid, $y_\alpha = y_E + \alpha\Delta y$, $\tau^{(\beta)} = \beta\Delta\tau$, with integral and semi-integral values for α and β. Accordingly, the nodal values become

$$\eta_j^{(n)}, \quad u_j^{(n)}, \quad v_{j+(1/2)}^{(n+(1/2))}, \tag{B 1}$$

and we assume that depth values are available at every grid point. Difference versions of (2.10), (2.11) and (2.12) read

$$[\delta_\tau\{\eta - F^{-1}(h+\epsilon\eta)u\} = -\delta_y\{(h+\epsilon\eta)v\} + B]_j^{(n-(1/2))}, \tag{B 2}$$

$$\left[u - \frac{\epsilon}{2}F^{-1}(u^2 + (\overline{v}^{xt})^2) = F^{-1}\eta + \mu^2 h\left\{\frac{1}{3}F^{-2}c_i^2 h\left(1 - hF^{-2}c_i^2\right)^{-1} + \frac{1}{2}\right\}\delta_y(h\delta_y u) - \frac{1}{6}\mu^2 h^2\delta_y^2 u\right]_j^{(n)}, \tag{B 3}$$

$$\left[\delta_\tau v + \frac{\epsilon}{2}\delta_y(T + (\overline{u}^y)^2) = -\delta_y\eta + \frac{1}{2}\mu^2 h\delta_y^2(h\delta_\tau v) - \frac{1}{6}\mu^2 h^2\delta_y^2\delta_\tau v \right.$$
$$+\frac{1}{3}\mu^2 F^{-2}c_i^2 h^2\delta_y\{(1 - hc_i^2F^{-2})^{-1}\delta_y(h\delta_\tau v)\}$$
$$\left. + \frac{1}{2}\mu^2 F^{-2}c_i^2 h\delta_y h(1 - hc_i^2F^{-2})^{-1}\delta_y(h\delta_\tau v) + D\right]_{j+(1/2)}^{(n)}, \quad \text{(B 4)}$$

where

$$[T^{(n)} = (\overline{v}^y)^{(n-(1/2))}(\overline{v}^y)^{(n+(1/2))}]_{j+(1/2)}, \quad \text{(B 5)}$$

and B and D are numerical correction terms that read

$$\left[B = \delta_y\left\{\frac{\Delta\tau^2}{24}h\delta_y\delta_\tau\eta - \frac{\Delta y^2}{24}\delta_y((1 - F^{-2}h)\delta_\tau\eta)\right\}\right]_j^{(n-(1/2))}, \quad \text{(B 6)}$$

$$\left[D = \frac{\Delta\tau^2}{24}\delta_y\{(1 - F^{-2}h)^{-1}\delta_y(h\delta_\tau v)\} - \frac{\Delta y^2}{24}\delta_y^2\delta_\tau v\right]_{j+(1/2)}^{(n)}. \quad \text{(B 7)}$$

The inclusion of B and D removes second-order discretization errors from the hydrostatic, linear parts (of the order of $\epsilon^0\mu^0$) of the equations. This gives a numerical accuracy similar to that obtained by Kennedy *et al.* (2000), Lynett *et al.* (2002) and Løvholt *et al.* (2008) (see discussion in Pedersen & Løvholt 2008). For each time increment, we solve all three difference equations simultaneously. We use an iteration procedure that treats all links through zeroth-order terms (in μ and ϵ) implicitly at each iteration level, while some of the remaining couplings are given Jacobi/Gauss–Seidel-like representations. The matter is then reduced to repeated solution of linear, three diagonal systems of equations. The discrete Eulerian equations are solved with boundary conditions corresponding to impermeable walls or input from other models, such as the Lagrangian one presented subsequently. An impermeable wall may be located at the $y_{N-(1/2)}$, say, with the computational domain limited by $y < y_{N-(1/2)}$. Then, we set $v_{N-(1/2)}^{(n+(1/2))} = 0$ and apply the symmetry condition $u_N^{(n)} = u_{N-1}^{(n)}$ in (B 4). On the other hand, if we have an input boundary at y_I, with an Eulerian domain limited by $y > y_I$, we specify u and η at node I and v at node $I + (1/2)$.

B.2. *Lagrangian marching procedure*

Now, we again switch to the scaling (2.1). In Lagrangian coordinates, we have four unknowns, namely y, H, u and v, which are determined by the set (2.14), (2.17), (2.18) and (2.19). As discrete unknowns, we employ

$$y_{j+(1/2)}^{(n)}, \quad H_j^{(n)}, \quad u_j^{(n)}, \quad v_{j+(1/2)}^{(n+(1/2))}, \quad \text{(B 8)}$$

where an index j now refers to the Lagrangian coordinate $a_j = j\Delta a$. The discrete equations then read

$$\left[\left(1 - \frac{\overline{u}^{a\tau}}{F}\right)\delta_\tau y = v\right]_{j+(1/2)}^{(n-(1/2))}, \quad \text{(B 9)}$$

$$\left[\left(1 - \frac{u}{F}\right)H\delta_a y = K\right]_j^{(n)}, \quad \text{(B 10)}$$

$$\left[u = -\frac{1}{2F}((\overline{v}^{a\tau})^2 + u^2) + \frac{1}{F}\{H - h(\overline{y}^a)\}\right]_j^{(n)}, \quad \text{(B 11)}$$

$$\left[\left(1-\frac{\overline{u}^a}{F}\right)\delta_\tau v = -\left(1-\frac{\overline{u}^a}{F}\right)\frac{\overline{H}^a}{\overline{K}^a}\delta_a H + \frac{\mathrm{d}h(y)}{\mathrm{d}y}\right]_{j+(1/2)}^{(n)}, \tag{B 12}$$

where the depth gradient term in (B 12) is computed by differences as in Jensen *et al.* (2003). In the present study, this is of minor consequence since the Lagrangian model is generally employed in regions where the depth gradient is constant. When $F \to \infty$ (normal incidence), the discrete equations yield explicit time integration. However, when u is non-zero, iteration must be employed. In the computational step that advances the discrete solution from $\tau = (n-(1/2))\Delta\tau$ to $\tau = (n+(1/2))\Delta\tau$, we first assign $u_j^{(n-1)}$ as start values for $u_j^{(n)}$. In each iteration cycle, we then compute new (and improved) generations of values according to the scheme (subscripts are omitted): New $y^{(n)}$ are found from (B 9) and new $H^{(n)}$ are computed by (B 10). Then, $v^{(n+(1/2))}$ are updated through (B 12). Finally, new $u^{(n)}$ are found by inserting the last available values into the right-hand side of (B 11).

At an input boundary, with location $a = a_L = (N-(1/2))\Delta a$, we must specify the values for $v_{N-(1/2)}$ and u_N, which may be provided by, for instance, the Eulerian model. The position of the u_N node is then determined by linear extrapolation from $y_{N-(3/2)}$ and $y_{N-(1/2)}$. If we have a shoreline at $a=0$, we set $H_0 = 0$. In addition, we define $u_0 = 2u_1 - u_2$ and $v_{-1/2} = (3/2)v_{1/2} - v_{3/2}$. The first of these fictitious values is required when $F < \infty$, while the τ-integral of the latter is needed in the depth gradient term of (B 12) for curved beach profiles.

B.3. *Model coupling*

A key idea in the solution procedure employed herein is the combination of the dispersive, Eulerian equations in finite depth and the Lagrangian NLSW equations near-shore. To this end, we employ overlapping domains and Schwartz iteration. The exchange of boundary conditions is enhanced by the common temporal resolution in the Eulerian and Lagrangian models. However, the spatial resolutions will not coincide and linear interpolations are then used in y and a, respectively. In the case $F = \infty$, $\epsilon = \mu = 0$, the exchange of data may be made only once, provided the overlap is larger than the wave speed times $\Delta\tau$. However, in the general case, we must employ iterations on implicit equations in each domain. After each internal iteration, we then extract updated boundary values for the adjacent domain in a modified Schwartz iteration. Similar procedures are elaborated by Glimsdal, Pedersen & Langtangen (2004).

Only values obtained solely from internal nodes should be exported from a grid. This imposes a minimum overlap. If we mark the Lagrangian and Eulerian grids by the superscripts L and E, respectively, it is required that

$$y_I^{(E)} \leqslant (\overline{y}^a)_{N-1}^{(L)}, \quad y_{I+(1/2)}^{(E)} \leqslant y_{N-(3/2)}^{(L)}, \quad y_{N-(1/2)}^{(L)} \geqslant y_{I+(3/2)}^{(E)}, \tag{B 13}$$

where I and N denote the boundaries of the two grids, respectively, and the Eulerian grid is located to the right (larger y). However, as shown by Glimsdal *et al.* (2004), a larger overlap may yield better performance for implicit equations, whereas a too large overlap is undesirable due to slight differences in wave celerity in the domains. Hence, the overlap is preferably kept at roughly the same size throughout a simulation. Initially, the Lagrangian grid is generally confined to a small near-shore region. During runup, the whole Lagrangian grid may be moved onshore and additional points must be activated in the Eulerian grid to maintain a good overlap. During drawdown, Eulerian points must correspondingly be exempted. Near the equilibrium shoreline, h is small and the dispersion ($O(\mu^2)$) terms in the Boussinesq momentum equations (2.11) and (2.12) are small. However, in a combined simulation, the Boussinesq equations may be invoked far inshore with relatively large negative values of h. The dispersion terms, as written in (2.11) and (2.12), may then give an appreciable, artificial effect. To avoid this, negative h values are replaced by zeros. As a consequence, the set (2.10)–(2.12) becomes the NLSW set onshore. Testing shows that in most cases the difference between keeping a negative h or replacing it by zero is small.

The procedure of exchanging boundary condition will generally suffice to produce good results. However, due to differences in mathematical and numerical properties in the two domains, the results in the overlap may deviate slightly. When the Eulerian grid is shrunk or extended, thereby changing the positions where values from the Lagrangian domain are imposed as boundary conditions, this will produce a moderate noise that becomes discernible in grid-refinement tests, for instance. One way to obtain a smoother transition is to apply a relaxation zone. In the momentum equation for the Eulerian velocity v_E, say, a term in $-\kappa(v_E - v_L)$ is added on the right-hand side. Here v_L is the Lagrangian velocity interpolated onto the Eulerian grid and the factor κ varies from unity to zero across the overlap zone. However, this strategy is presumably not fully effective in the present context, where the overlap zone moves and extends/shrinks abruptly. Instead, a global solution is defined through a weighted average in the overlap, with the weighing going linearly from purely Lagrangian near-shore to purely Eulerian at the other end. Precedence is given to the near-shore region such that the Eulerian field variables are replaced by the global solution in the overlap. This procedure reduces the noise substantially.

B.4. *The linear model*

The leading-order equations, which are linear and non-dispersive, are obtained by putting $\mu=\epsilon=0$ in (2.10)–(2.12). We may then eliminate the velocities to obtain a single wave equation

$$\frac{\partial^2\eta}{\partial\tau^2} - \left(1 - F^{-2}h\right)^{-1}\frac{\partial}{\partial y}\left(h\frac{\partial\eta}{\partial y}\right) = 0, \tag{B 14}$$

where an extra coefficient has appeared in front of the spatially differentiated term as compared to the case of normal incidence. In Pedersen (1985) and Koshimura, Imamura & Shuto (1999), an equation equivalent to (B 14) is solved for a periodic incident wave. For single pulses of certain shapes, such as a Gaussian bell or a solitary wave given by a squared hyperbolic secant, a Fourier transform may be applied (see Carrier & Noiseux 1983). However, this approach will involve the numerical inversion of integrals of expressions involving the Kummer function. A finite-difference solution of (B 14) is preferred herein because it is simpler, more general, and, in fact, involves less numerics.

Equation (B 14) is discretized by the standard five-point, explicit method

$$\left[\delta_\tau^2\eta - \left(1 - F^{-2}h\right)^{-1}\delta_y(h\delta_y\eta) = 0\right]_j^{(n)}. \tag{B 15}$$

Assuming the shoreline to be located at $y=0$, we obtain the best performance by defining the grid according to $y_j=(j-(1/2))\Delta y$. Then $y_1^{(n)}$, located at $y=(1/2)\Delta y$, is the surface node closest to the shoreline. For $j=1$, the shoreward flux term in (B 15), which involves $\eta_0^{(n)}$, then becomes zero because $h_{1/2}=h(0)=0$. Then, no boundary condition is needed for $\eta_0^{(n)}$ since this quantity does not couple to the wet nodes. This is the discrete counterpart to the common analytic condition of finite η at the shoreline, which more properly should be stated as zero volume flux.

While initial conditions are used for our primary, nonlinear model, a combined input/radiation condition is used for (B 15). The condition is invoked in constant depth $h = 1$ and the analytic version reads

$$\frac{\partial \eta}{\partial \tau} + (\cos\theta_i)^{-1}\frac{\partial \eta}{\partial y} = 2Y', \tag{B 16}$$

where $Y(\cos\theta_i y + \tau)$ defines the incident wave, which has celerity equal to one in the linear approximation. Any wave propagating in the positive y-direction will be transmitted out of the computational domain without reflection. The form function Y may be the one referred to at the end § 2.3 or given by (3.1). The relative differences in the runup heights are small. For $\phi = 10.54°$, differences increase from 0.0006 to 0.0023, roughly, when the amplitude is increased from $A = 0.05$ to $A = 0.25$. The profile from the formula (KdV soliton) is wider near the crest and narrower at the base and yields the smaller R/A. In the computations, (3.1) is used. The discrete version of (B 16) reads as

$$[\delta_\tau \overline{\eta}^y + (\cos\theta_i)^{-1}\delta_y \overline{\eta}^\tau = P]_{N+(1/2)}^{(n+(1/2))}, \tag{B 17}$$

where P is evaluated by inserting the incident wave into the left-hand side. The choice of N is restricted by $N\Delta y \geqslant \cot\phi$, which ensures that $\eta_{N-(1/2)}$ in principle may be linked to the constant depth region, without involving non-unitary depths.

REFERENCES

Briggs, M. J., Synolakis, C. E., Harkins, G. S. & Green, D. R. 1995 Laboratory experiments of tsunami runup on a circular island. *Pure Appl. Geophys.* **144** (3–4), 569–593.

Brocchini, M. 1998 The run-up of weakly-two-dimensional solitary pulses. *Nonlinear Processes Geophys.* **5**, 27–38.

Brocchini, M., Kennedy, A., Soldini, L. & Mancinelli, A. 2004 Topographically controlled, breaking-wave-induced macrovortices. Part 1. Widely separated breakwaters. *J. Fluid Mech.* **507**, 289–307.

Brocchini, M. & Peregrine, D. H. 1996 Integral flow properties of the swash zone and averaging. *J. Fluid Mech.* **317**, 241–273.

Bühler, O. & Jacobson, T. E. 2001 Wave-driven currents and vortex dynamics on barred beaches. *J. Fluid Mech.* **449**, 313–339.

Carrier, G. F. & Greenspan, H. P. 1958 Water waves of finite amplitude on a sloping beach. *J. Fluid Mech.* **4**, 97–109.

Carrier, G. F. & Noiseux, C. F. 1983 The reflection of obliquely incident tsunamis. *J. Fluid Mech.* **133**, 147–160.

Carrier, G. F., Wu, T. T. & Yeh, H. 2003 Tsunami run-up and draw-down on a plane beach. *J. Fluid Mech.* **475**, 79–99.

Choi, B. H., Pelinovsky, E., Kim, D. C., Didenkulova, I. & Woo, S.-B. 2008 Two- and three-dimensional computation of solitary wave runup on non-plane beach. *Nonlinear Processes Geophys.* **15**, 489–502.

Didenkulova, I. 2008 New trends in the analytical theory of long sea wave runup. In *Applied Wave Mathematics: Selected Topics in Solids, Fluids, and Mathematical Methods*, pp. 265–296. Springer.

Didenkulova, I., Pelinovsky, E., Soomere, T. & Zahibo, N. 2007 Runup of nonlinear asymmetric waves on a plane beach. In *Tsunami and Nonlinear Waves* (ed. A. Kundu), pp. 175–190. Springer.

Glimsdal, S., Pedersen, G. & Langtangen, H. P. 2004 An investigation of overlapping domain decomposition methods for one-dimensional dispersive long wave equations. *Adv. Water Resour.* **27** (11), 1111–1133.

Grilli, S., Svendsen, I. & Subramanya, R. 1997 Breaking criterion and characteristics for solitary waves on slopes. *ASCE J. Waterway Port Coastal Ocean Engng* **123** (3), 102–112.

GUZA, R. T. & DAVIS, R. E. 1974 Excitation of edge waves by waves incident on a beach. *J. Geophys. Res.* **79**, 1285–1291.

HALL, J. V. & WATTS, J. W. 1953 Laboratory investigation of the vertical rise of solitary waves on impermeable slopes. *Tech. Memo.* 33. Beach Erosion Board, US Army Corps of Engineers.

IMAMURA, F. 1996 Review of tsunami simulation with a finite difference method. In *Long-Wave Runup Models* (ed. H. Yeh, C. E. Synolakis & P. L.-F. Liu), pp. 25–42. World Scientific.

JENSEN, A., PEDERSEN, G. & WOOD, D. J. 2003 An experimental study of wave run-up at a steep beach. *J. Fluid. Mech.* **486**, 161–188.

KÂNOĞLU, U. & SYNOLAKIS, C. E. 1998 Long-wave runup on piecewise linear topographies. *J. Fluid Mech.* **374**, 1–28.

KELLER, H. B., LEVINE, A. D. & WHITHAM, G. B. 1960 Motion of a bore over a sloping beach. *J. Fluid Mech.* **7**, 302–316.

KENNEDY, A. B., CHEN, Q., KIRBY, J. T. & DALRYMPLE, R. A. 2000 Boussinesq modeling of wave transformation, breaking, and run-up. Part I. 1D. *ASCE J. Waterway Port Coastal Ocean Engng* **126** (1), 39–47.

KO, K. & KUEHL, H. H. 1979 Cylindrical and spherical Korteweg–deVries solitary waves. *Phys. Rev. Lett.* **22**, 1343–1348.

KOSHIMURA, S., IMAMURA, F. & SHUTO, N. 1999 Propagation of obliquely incident tsunamis on a slope. Part I. Amplification of tsunamis on a continental slope. *Coast. Engng J.* **41** (2), 151–164.

LEVEQUE, R. J. & GEORGE, D. L. 2008 High-resolution finite volume methods for the shallow water equations with bathymetry and dry states. In *Advanced Numerical Models for Simulating Tsunami Waves and Runup* (ed. P. L.-F. Liu, H. Yeh & C. E. Synolakis), vol. 10, pp. 43–74. World Scientific.

LI, Y. & RAICHLEN, F. 2001 Solitary wave runup on plane slopes. *ASCE J. Waterway Port Coastal Ocean Engng* **127** (1), 33–44.

LIU, P. L.-F., CHO, Y.-S., BRIGGS, M. J., KÂNOĞLU, U. & SYNOLAKIS, C. E. 1995 Runup of solitary waves on a circular island. *J. Fluid Mech.* **302**, 259–285.

LIU, P. L.-F., YEH, H. & SYNOLAKIS, C. E. (Ed.) 2008 *Advances in Coastal and Ocean Engineering*, vol. 10. World Scientific.

LYNETT, P. J., WU, T.-R. & LIU, P. L.-F. 2002 Modeling wave runup with depth-integrated equations. *Coast. Engng* **46**, 89–107.

LØVHOLT, F. L. & PEDERSEN, G. 2009. Instabilities of Boussinesq models in non-uniform depth. *Numer. Meth. Fluid Mech.* **61** (6), 606–637, doi:10.1002/fld.1968.

LØVHOLT, F. L., PEDERSEN, G. & GISLER, G. 2008 Oceanic propagation of a potential tsunami from the La Palma Island. *J. Geophys. Res.* **113**, C09026, doi:10.1029.

MADSEN, P. A. & SCHÄFFER, H. A. 1999 A review of Boussinesq-type equations for surface gravity waves. In *Advances in Coastal and Ocean Engineering*, vol. 5, pp. 1–95. World Scientific.

MEYER, R. E. & TAYLOR, A. D. 1972 *Run-up on Beaches*, pp. 95–122. Academic Press.

MILES, J. W. 1977*a* Diffraction of solitary waves. *Z. Angew. Math. Phys.* **28**, 889–902.

MILES, J. W. 1977*b* Obliquely interacting solitary waves. *J. Fluid Mech.* **79**, 157–169.

MILES, J. W. 1977*c* Resonantly interacting solitary waves. *J. Fluid Mech.* **79**, 171–179.

MILES, J. W. 1980 Solitary waves. *Annu. Rev. Fluid Mech.* **12**, 11–43.

PEDERSEN, G. 1985 *Run-up of Periodic Waves on a Straight Beach.* Preprint Series in Applied Mathematics, ISBN 82-553-0952-7 1/85. Department of Mathematics, University of Oslo, Norway.

PEDERSEN, G. 1988 Three-dimensional wave patterns generated by moving disturbances at transcritical speeds. *J. Fluid Mech.* **196**, 39–63.

PEDERSEN, G. 1994 Nonlinear modulations of solitary waves. *J. Fluid Mech.* **267**, 83–108.

PEDERSEN, G. 1996 Refraction of solitons and wave jumps. In *Waves and Nonlinear Processes in Hydrodynamics* (ed. B. Gjevik, J. Grue & J. E. Weber), pp. 139–150. Kluwer.

PEDERSEN, G. 2008*a* A Lagrangian model applied to runup problems. In *Advanced Numerical Models for Simulating Tsunami Waves and Runup* (ed. P. L.-F. Liu, H. Yeh & C. E. Synolakis), pp. 311–314. Advances in Coastal and Ocean Engineering, vol. 10. World Scientific.

PEDERSEN, G. 2008*b* Modeling run-up with depth-integrated equation models. In *Advanced Numerical Models for Simulating Tsunami Waves and Runup* (ed. P. L.-F. Liu, H. Yeh & C. E. Synolakis), pp. 3–42. Advances in Coastal and Ocean Engineering, vol. 10. World Scientific.

Pedersen, G. & Gjevik, B. 1983 Run-up of solitary waves. *J. Fluid Mech.* **135**, 283–299.

Pedersen, G. & Løvholt, F. L. 2008 *Documentation of a Global Boussinesq Solver*. Preprint Series in Applied Mathematics 1. Department of Mathematics, University of Oslo, Norway. Available at: http://www.math.uio.no/eprint/appl_math/2008/01-08.html.

Peregrine, D. H. 1972 Equations for water waves and the approximation behind them. In *Waves on Beaches* (ed. R. E. Meyer), pp. 357–412. Academic Press.

Peregrine, D. H. 1983 Wave jumps and caustics in the propagation of finite-amplitude water waves. *J. Fluid Mech.* **136**, 435–452.

Peregrine, D. H. 1998 Surf zone currents. *Theor. Comput. Fluid Dyn.* **10**, 295–309.

Pritchard, D. & Dickinson, L. 2007 The near-shore behaviour of shallow-water waves with localized initial conditions. *J. Fluid Mech.* **591**, 413–436.

Reutov, V. A. 1976 Behaviour of perturbations of solitary and periodic waves on the surface of a heavy liquid. *Fluid Dyn.* **11**, 778–781.

Ryrie, S. C. 1983 Longshore motion generated on beaches by obliquely incident bores. *J. Fluid Mech.* **129**, 193–212.

Shen, M. C. & Meyer, R. E. 1963 Climb of a bore on a beach. Part 3. Run-up. *J. Fluid Mech.* **16**, 113–125.

Synolakis, C. E. 1987 The run-up of solitary waves. *J. Fluid Mech.* **185**, 523–545.

Tadepalli, S. & Synolakis, C. 1994 The run-up of N-waves on sloping beaches. *Proc. R. Soc. Lond.* A **445**, 99–112.

Thacker, W. C. 1981 Some exact solutions to the nonlinear shallow-water wave equations. *J. Fluid Mech.* **107**, 499–508.

Titov, V. V. & Synolakis, C. E. 1998 Numerical modeling of tidal wave runup. *ASCE J. Waterway Port Coastal Ocean Engng* **124** (4), 157–171.

Wei, G., Kirby, J. T., Grilli, S. T. & Subramanya, R. 1995 A fully nonlinear Boussinesq model for surface waves. Part 1. Highly nonlinear unsteady waves. *J. Fluid Mech.* **294**, 71–92.